



Hybridization-based sensor with large dynamic range for detection of circulating tumor DNA in clinical samples

Yannick Stulens^{a,1}, Rebekka Van Hoof^{a,b,c,1}, Karen Hollanders^{b,1}, Inge Nelissen^{b,1}, Michal Szymonik^{b,1}, Patrick Wagner^{c,1}, Guy Froyen^{d,e,1}, Brigitte Maes^{d,e,1}, Jef Hooyberghs^{a,1,*}

^aUHasselt, Data Science Institute, Theory Lab, Agoralaan, Diepenbeek, 3590, Belgium

^bFlemish Institute for Technological Research (VITO), Environmental Intelligence Unit, Mol, 2400, Belgium

^cKU Leuven, Faculty of Science, Department of Physics and Astronomy, Laboratory for Soft Matter and Biophysics, Celestijnenlaan 200 D, Leuven, 3001, Belgium

^dJessa Hospital, Laboratory for Molecular Diagnostics, Department of Clinical Biology, Hasselt, 3500, Belgium

^eUHasselt, Faculty of Medicine and Life Sciences, Agoralaan, Diepenbeek, 3590, Belgium

ARTICLE INFO

Keywords:

Hybridization-based biosensor
Low-abundance mutant detection
Dynamic range extension
DNA thermodynamics
Liquid biopsy
Clinical NSCLC samples

ABSTRACT

In a liquid biopsy approach, targeted mutation analysis of circulating tumor DNA (ctDNA) is a valuable tool for diagnosis, monitoring and personalization of therapy. The ctDNA usually makes up only a small fraction of the total circulating free DNA (cfDNA), and ctDNA often only differs from cfDNA at a single nucleotide. This sets strong requirements on the analytical performance of hybridization-based biosensors, which is the focus of this paper. We use clinical samples and apply the concept of wild-type target depletion. Along with this, we develop an accurate thermodynamic theory for the competitive hybridization and use it for selecting optimal experimental conditions and for data analysis. The result is a biosensor with improved quantification of ctDNA mutations, both the sensitivity and dynamic range are improved by an order of magnitude. As reference techniques, we used a clinically-validated real-time PCR assay and digital PCR for absolute quantification. Our approach can be applied to a broad range of hybridization-based biosensors, providing a robust and effective method to improve the performance of existing biosensors.

1. Introduction

The use of biosensors for clinical applications has increased greatly in recent years (Lino et al., 2022). Biosensors research is driven by clinical needs, and new research influences clinical practice. An important example is the need to detect somatic gene variants for cancer diagnosis, prognosis, and treatment monitoring. While tissue biopsy is the standard for genetic profiling of tumors, analyzing circulating free DNA (cfDNA) in liquid samples, such as blood, offers a less invasive alternative (Abbosh et al., 2017; Xie et al., 2023). Known as liquid biopsy (LB), this approach enables frequent testing and at the same time reduces discomfort, risk and cost. LB also overcomes the limitations of tissue biopsy, which may miss tumor heterogeneity (García-Pardo et al., 2022; Udomruk et al., 2021). Studies highlight circulating tumor DNA (ctDNA) as a valuable biomarker for survival, mutational burden, and treatment benefit for different tumor types (Lu et al., 2024; Sivapalan et al., 2023; Zhou et al., 2023).

From a biosensor point-of-view, it is important to pinpoint the analytical challenge associated with its application in oncogene mutant detection. Tumor-derived ctDNA (mutant), is present in an abundance of cfDNA from healthy cells (wild-type). Often, mutant and wild-type sequences differ in only a single nucleotide and ctDNA represents only a small fraction of the total cfDNA, less than 0.1% in early stages of tumor development (Alese et al., 2022). By its classical definition, a biosensor is an analytical device composed of a biological sensing element in intimate contact with a physical transducer, which together relate the concentration of an analyte to a measurable signal. With the LB application in mind, however, it is not just the concentration of the analyte, but the *relative* concentration of mutant over wild-type that poses the new challenge. This increases the importance of the biological sensing element of the biosensor, because it must be able to distinguish between two very similar molecules present in a very asymmetric abundance. In many sensitive detection techniques, the biological sensing element is a DNA probe, hybridizing with the clinical

* Corresponding author.

E-mail address: jef.hooyberghs@uhasselt.be (J. Hooyberghs).

¹ These authors contributed equally to this work.

target DNA sequence. This basic process is the focus of this work, showing how the quantification of the relative mutant concentration can be improved, both in its sensitivity and dynamic range.

In current clinical practice, detection of single nucleotide variants (SNVs) is typically achieved with real-time polymerase chain reaction (PCR), digital PCR (dPCR) for single gene analyses, and targeted next-generation sequencing for multigene testing, but for cfDNA analysis, sensitivity remains an issue irrespective of the used technique and body fluid type (Alexandrou et al., 2023; Ferrara et al., 2022; Silveira et al., 2021; Takahashi et al., 2023; Wang et al., 2021). The use of direct hybridization-based biosensors has increased, both in the number of applications and the diversity of its application conditions (Ferrara et al., 2022; Li et al., 2019; Zhuang et al., 2022). Therefore, we study direct hybridization-based biosensing for SNV quantification in cfDNA samples. The approach starts from the basic biological sensing element and does not depend on the specific readout technology of the biosensor. Here, we have chosen a mature and reliable technology with optical readout, namely microarrays, but the results of our work are easily transferable to a wide variety of sensing technologies, including multiplex and cost-effective biosensor devices (Alipour et al., 2020; Dillen et al., 2021; Magar et al., 2021; Mueller et al., 2023; Van Grinsven et al., 2011, 2012; Wei et al., 2023; Wood et al., 2019).

Hybridization-based sensors use single-stranded oligonucleotide probes to capture and bind DNA targets of interest. The detection of SNVs relies fundamentally on the difference in binding thermodynamics between perfectly complementary and partially mismatched DNA sequences. Here, knowledge about competitive hybridization of non-mutant target sequences to the probes is used to improve quantification of low-abundant mutations (Karadeema et al., 2018; Knez et al., 2013). The application of capture probes selected for their thermodynamic properties leads to the intentional depletion of the corresponding wild-type target. This methodology has previously been demonstrated to increase the sensitivity of hybridization-based SNV detection to a level comparable with current PCR-based benchmarking methods, and is therefore suitable for clinical applications of LB-based gene analysis (Hooberghs et al., 2010; Nomidis et al., 2019; Van Hoof et al., 2022; Willems et al., 2017). In the current work, we explore the sensitivity and the applicability of the methodology for the first time on LBs. We use clinical cfDNA samples from non-small cell lung cancer (NSCLC) patients that were tested for the p.T790M mutation of the epidermal growth factor receptor (*EGFR*). This biomarker is known to be associated with resistance to first- and second-generation tyrosine kinase inhibitor treatment (Wang et al., 2016). The detection of the mutation is done on an assay subject to wild-type target depletion, and compared to one without depletion capture probes. Both are in turn compared to two reference techniques: a clinically-validated real-time PCR and dPCR, which is considered the golden-standard technique for low-abundant mutant detection (Silveira et al., 2021; Zhang et al., 2015). A schematic overview of the workflow is presented in Supplementary Information S1. In addition, we expand the thermodynamic theory, enabling us to estimate mutant ratios from samples with both low and high relative mutant ratios. The expansion leads to important insights for future probe designs. This crucial step increases the dynamic range of the biosensor and consequently the range of applications (Cohen et al., 2023).

2. Materials and methods

2.1. Hybridization method: the reference probe and the concept of depletion

A hybridization-based sensor detects the presence of single-stranded (ss) mutant DNA by ssDNA hybridization probes. The detection is based on the formation of a stable double helix, where the two strands obey the Watson-Crick pairing rule. The binding of mutant target *T_{mut}* to the probe indicates the presence of mutant DNA. If the mutant DNA is present in a background of wild-type target *T_{wt}*, i.e. as a mix

in the same sample, the sensor's performance is impeded by cross-hybridization with wild-type targets. This cross-hybridization is most severe when *T_{mut}* is a SNV of *T_{wt}*, where only a single nucleotide differs between *T_{mut}* and *T_{wt}*. While traditionally, cross-hybridization leads to a reduced detection sensitivity, we will show in Section 2.1.1 how cross-hybridization allows one to define a robust mutant detection signal. More specifically, we focus on the situation where target sequences *T_{mut}* and *T_{wt}* are known, and we aim to detect a minority of mutant targets in a majority of wild-type background.

An important aspect of sensor design is the selection of probe sequences needed to detect mutant DNA in a sample. The mutant probe (*P_{mut}*) is designed to physically cover the mutant sequence in a region around the SNV with roughly a few dozens of nucleotides (see Section 2.6). In Sections 2.1.1 and 2.1.2, we explain how the use of additional probes improves performance of the hybridization-based sensor. These probes will either match the wild-type sequence (probe *P_{wt}*) or be used as a reference signal (probe *P_{ref}*).

When the hybridization between the sample targets and the probes has reached thermal equilibrium, the readout occurs. Many technologies and means are available for experimental readout, including fluorescence emission, changes in heat transfer resistance, or microgravimetric sensors (Van Grinsven et al., 2012; Yoshimine et al., 2023). We use microarray technology, which provides a mature sensing platform and enables readout spanning up to five orders of magnitude. In microarrays, probes are spatially organized into spots and targets are fluorescently labeled. The optical readout of a spot provides a fluorescent intensity *I*. For example, the intensity *I_{P_{mut}}* is proportional to the fraction of *P_{mut}* bound to a target, whether it is *T_{wt}*, *T_{mut}* or a combination of the two targets. Notably, no distinction can be made between *T_{wt}* or *T_{mut}* being bound to *P_{mut}*. This emphasizes the need for a reference probe, which is introduced in the next section.

2.1.1. Reference probes allow for a robust sensor design

To obtain a mutant-specific signal for sample mixtures, one can introduce an additional probe *P_{ref}* as a reference, which is designed in such a way that *T_{wt}* has an equal affinity toward the *P_{ref}* as it does toward the *P_{mut}*. An appropriate reference sequence can be found by exploring, theoretically and experimentally (Van Hoof et al., 2022), cross-hybridizations between different variants of the *P_{wt}*, containing one or two mismatches to *T_{wt}* (one or two nucleotide pairs that do not obey the Watson-Crick pairing rule). The reference probe then allows the mutant detection signal *S* to be defined as a robust ratiometric quantity, given by

$$S = \ln \left(\frac{I_{P_{mut}}}{I_{P_{ref}}} \right). \quad (1)$$

By design, if only *T_{wt}* is present, cross-hybridizations *T_{wt} + P_{mut}* and *T_{wt} + P_{ref}* will occur equally often, i.e. *I_{P_{mut}}* = *I_{P_{ref}}*, and the signal *S* will be zero. However, when some amount of mutant is present, *I_{P_{mut}}* will increase, and the signal will be positive, indicating the presence of mutant in the sample (Fig. 1A and B).

The mutant detection signal, given by Eq. (1), is described by standard Langmuir theory, which relates the occupancy of probes to target concentrations *c_{mut}/c_{wt}* and affinities between probes and targets (Harrison et al., 2013). At a low fractional abundance of the mutant target, the signal is described by:

Signal without depletion:

$$S_{no_depl} = \ln \left(1 + \frac{c_{mut}}{c_{wt}} \exp \left(\frac{\Delta\Delta G_{P_{mut}}}{RT} \right) \right) \quad (2)$$

where *R* is the universal gas constant, *T* is the absolute temperature and $\Delta\Delta G_{P_{mut}}$ represents the difference in hybridization free energy (ΔG) between the mutant probe and its two targets, mutant and wild-type. Notably, the sensor benefits from having a large $\Delta\Delta G_{P_{mut}}$, amplifying the mutant ratio *c_{mut}/c_{wt}* and increasing sensitivity. However, this free-energy difference is determined by the target sequences and it is not a design parameter. The following section will introduce a way to further improve the sensor performance, using the concept of depletion.

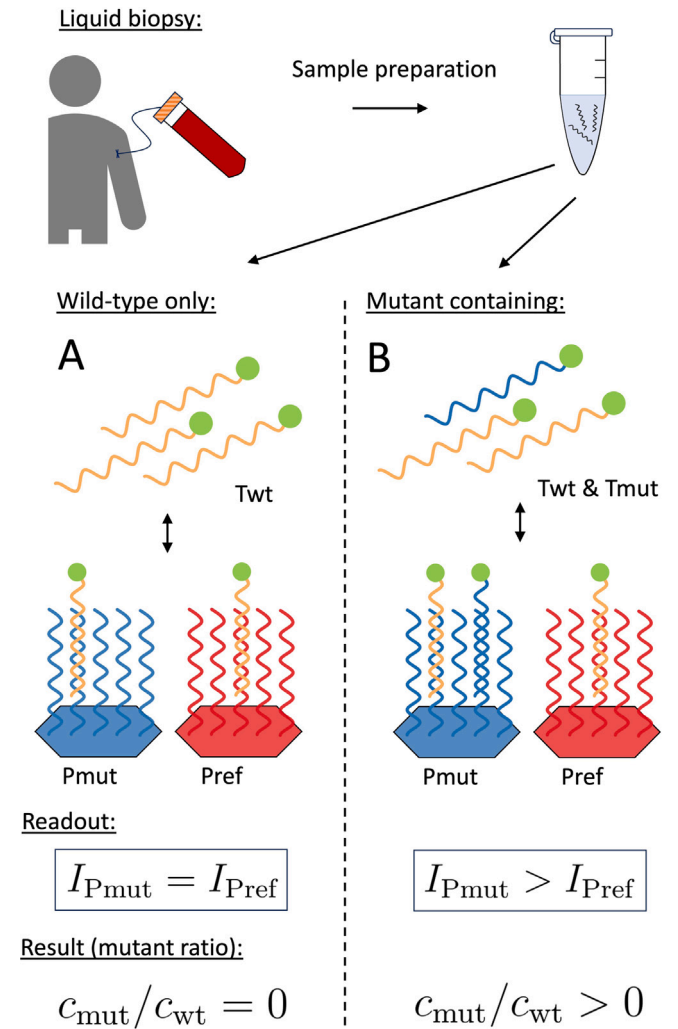


Fig. 1. Overview of the hybridization method-based mutant detection assay (Nomidis et al., 2019; Van Hoof et al., 2022). (A) When the assay is subject to a pure wild-type sample, the same amount of target will bind to *Pmut* and *Pref*, the intensity readout is the same and the mutant ratio is predicted to be zero. (B) When mutant DNA is present, the additional hybridization to *Pmut* will result in a higher intensity for *Pmut* compared to *Pref*. This signals the presence of mutant DNA.

2.1.2. Depletion probes enrich the mutant content in a sample

By introducing an abundance of wild-type matching probes *Pwt*, a large number of wild-type targets will bind to *Pwt* and become unable to contribute to the signal. The available amount of wild-type gets depleted. Of course, the available amount of mutant is also lowered, but by design there is a selective reduction of available target concentrations, such that the mutant ratio is enlarged to an effective ratio $c_{mut}^{eff}/c_{wt}^{eff}$. Because available concentrations are lowered, this usually requires an increase in total target concentration. Depletion by wild-type probes enriches the mutant content in the sample, which increases the ratio I_{Pmut}/I_{Pref} and the signal S (Fig. 2B). The enrichment is determined by the difference in free energy between the wild-type probe and its two targets *Twt* and *Tmut*, $\Delta\Delta G_{Pwt}$. When the affinity to wild-type probes is high, a condition we call strong depletion (Nomidis et al., 2019), the enrichment of the mutant ratio reaches the theoretical maximum of a factor $\exp(\Delta\Delta G_{Pwt}/RT)$, and consequently the signal is maximally enhanced and given by:

Signal with depletion:

$$S_{depl} = \ln \left(1 + \frac{c_{mut}}{c_{wt}} \exp \left(\frac{\Delta\Delta G_{Pmut} + \Delta\Delta G_{Pwt}}{RT} \right) \right) \quad (3)$$

Depletion of wild-type targets further increases sensitivity and produces a higher signal when mutant targets are present in the sample compared to the no-depletion case (Eq. (2)). As in our previous work, the limit of detection (LoD) is defined as the mutant fractional abundance corresponding to a signal equal to three times the standard deviation of a pure wild-type negative control sample (Van Hoof et al., 2022). The higher signal in case of target depletion results in an improved LoD.

2.1.3. Hybridization assay allows determination of mutant content

In the hybridization experiment, the intensities of the mutant and reference probes are measured, and their ratio is used to determine the signal via Eq. (1). Fig. 2C shows the theoretical signals of the hybridization assays as a function of the mutant ratio c_{mut}/c_{wt} , Eqs. (2) and (3). Conversely, one can invert the equation of signal S to allow the determination of the mutant ratio c_{mut}/c_{wt} in a sample after experimental measurement. The mutant ratio of the sample is calculated using Eqs. (4) and (5). In Section 3.3, we will show that these equations are only valid for samples with low signals or mutant ratios, and that accurate determination of the mutant ratio for high signals requires an extension to the model concerning the interaction between *Tmut*+*Pref*.

No-depletion:

$$\frac{c_{mut}}{c_{wt}} = (\exp(S_{no_depl}) - 1) \exp \left(-\frac{\Delta\Delta G_{Pmut}}{RT} \right) \quad (4)$$

Depletion:

$$\frac{c_{mut}}{c_{wt}} = (\exp(S_{depl}) - 1) \exp \left(-\frac{\Delta\Delta G_{Pmut} + \Delta\Delta G_{Pwt}}{RT} \right) \quad (5)$$

In this article, we use the same design as in our previous work (Van Hoof et al., 2022), where we showed that adding depletion probes improves the detection sensitivity of the *EGFR* T790M mutation using synthetic DNA samples and surface-tethered probes. Synthetic DNA samples of differing mutant ratios were used to perform a least-square fit to Eqs. (2) and (3), and free energies $\Delta\Delta G_{Pmut}/RT$ and $\Delta\Delta G_{Pwt}/RT$ were obtained. These values, determined to be 4.7 and 1.86 respectively, were in close agreement with values expected from thermodynamic nearest-neighbor parameters (Hadiwikarta et al., 2012) and are used throughout this article. The LoD was determined to be $c_{mut}/c_{wt} = 0.0060$ ($c_{mut}/c_{tot} \approx 0.60\%$) under the no-depletion condition and improved to $c_{mut}/c_{wt} = 0.00048$ ($c_{mut}/c_{tot} \approx 0.048\%$) in the depletion case (Van Hoof et al., 2022). When c_{mut}/c_{wt} is below the LoD, samples are classified as negative. Details of the experimental implementation are given in Section 2.6.

2.2. NSCLC patients' cfDNA samples

Leftover cfDNA from 18 NSCLC patients were obtained from the Jessa Hospital (Hasselt, Belgium) with ethical approval of the Ethics Review Committee of the Jessa Hospital under code 2021/023. The QiAamp circulating nucleic acid kit (Qiagen, Hilden, Germany, #55114) was used for extraction of cfDNA and residual samples were stored for up to 3 years at -20°C in DNA LoBind tubes (Eppendorf). A volume of 30 - 35 μL per sample was received together with information on their *EGFR* c.2369C>T p.(T790M) mutational status based on real-time PCR (using the *EGFR* Mutation analysis kit from EntroGen, Woodland Hills, CA, #EGFR-RT52 and a Rotor-Gene X device from Qiagen) performed on freshly extracted cfDNA by the Jessa Hospital as part of their molecular diagnostic workflow. In the clinical assay, a threshold cycle (C_t) value of the housekeeping gene beta-2-microglobulin (B2M) reaction was subtracted from the C_t value for *EGFR* T790M in order to determine a delta C_t (ΔC_t) value.

$$\Delta C_t = C_{tT790M} - C_{tB2M} \quad (6)$$

EGFR T790M samples were classified as positive when the $\Delta C_t \leq 7.4$. According to this criterion, six samples were classified as positive and twelve as negative in the real-time PCR clinical assay. Clinical diagnostic information is provided in Supplementary Information S2.

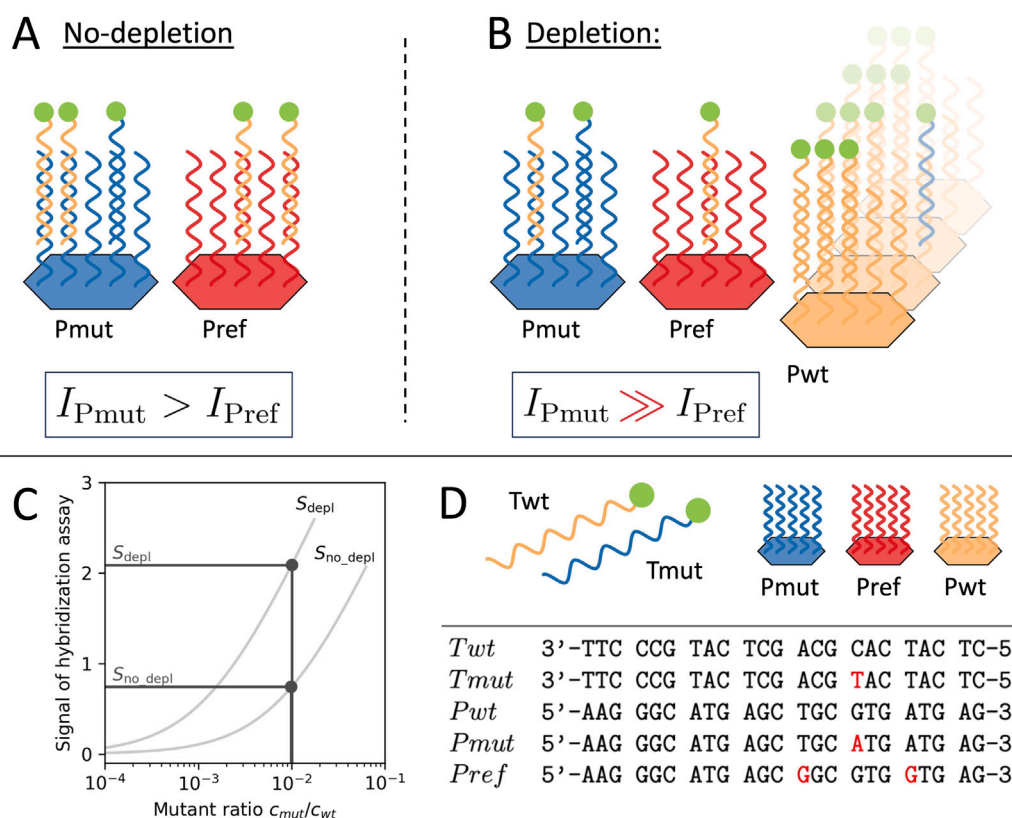


Fig. 2. The concept of depletion in the hybridization method (Nomidis et al., 2019; Van Hoof et al., 2022). (A) and (B) When a large amount of wild-type target depletion probes *Pwt* are present, the difference between the *Pmut* and *Pref* intensities becomes larger. (C) Theoretical predicted signal of the hybridization assay under depletion condition (S_{depl} , Eq. (3)) and no-depletion condition (S_{no_depl} , Eq. (2)) in terms of mutant ratio c_{mut}/c_{wt} . Vertical lines demonstrate how the same mutant ratio results in a larger signal in the depletion case. Horizontal lines show how an experimental measurement of the signal can be used to obtain the mutant ratio. (D) Target and probe sequences used in the hybridization experiments. Only the 23 bp probe binding region is shown for the clinical NSCLC targets. Differences between the wild-type target sequence or the wild-type probe sequence are highlighted in red.

2.3. dPCR

A QX200 Droplet Digital PCR System (ddPCR, Bio-Rad Laboratories, Hercules, CA) was used to perform dPCR-based mutation detection of the *EGFR* 790M mutation. The reaction mixture contained 11 μ L 2 \times ddPCR supermix for probes (No dUTP, Bio-Rad Laboratories, #1863023), 1.1 μ L 20 \times primers and probes (Bio-Rad Laboratories, assay ID: dHsaMDV2010019), 2.4 μ L nuclease-free water and 7.5 μ L of cfDNA sample or no-template control (NTC). Droplets were generated using the QX200TM Droplet Generator and transferred to a 96-well plate before sealing the plate using the PX1 PCR Plate Sealer according to the manufacturer's instructions. For PCR, the following amplification conditions were used: 95 $^{\circ}$ C for 10 min; 40 cycles of 94 $^{\circ}$ C for 30 s, 55 $^{\circ}$ C for 1 min and 98 $^{\circ}$ C for 10 min at a temperature ramp rate of 2 $^{\circ}$ C/second and a C1000 TouchTM Thermal Cycler with 96-deep well reaction module were used. After the amplification, the plate was kept at 4 $^{\circ}$ C for 30 min. A QX200TM Droplet Reader was used for the fluorescence intensity readout and results were analyzed using QuantaSoftTM Analysis Pro 1.0.596 Software (Bio-Rad Laboratories). For analysis, the inclusion criterion was $\geq 10,000$ droplets/well and fluorescence thresholds for the *EGFR* assay were set at 2275.10 for channel 1 (mutant) and 2051.14 for channel 2 (wild-type). Droplet counts and mutant ratios of the clinical samples with corresponding confidence intervals calculated by the software are presented in Supplementary Information S3.

2.4. PCR amplicon generation

For DNA hybridization experiments, amplicons of the NSCLC cfDNA samples of 107 bp comprising the region of the *EGFR* T790M mutation were generated. The PCR reaction mixture contained 25 μ L

2 \times PlatinumTM II Hot-Start PCR Master Mix (Invitrogen, ThermoFisher Scientific, Merelbeke, Belgium, #14000013), 2.5 μ L forward primer (10 μ M): 5' ATC TGC CTC ACC TCC AC 3', 2.5 μ L reverse primer (10 μ M) with 5'-end phosphate modification: 5' /Phos/ CTG GCG TCA TAG CTG TTT CCT GTG TGA TTG TGT TCC CGG ACA TAG TC 3', 12.5 μ L nuclease-free water and 7.5 μ L cfDNA sample. A 1.0% mixture of *EGFR* T790M mutation in a wild-type background of 500 bp gBlocksTM Gene Fragments (IDT, Leuven, Belgium) and nuclease-free water as NTC were taken along as positive and negative control, respectively. The sequence is available in Supplementary Information S4. Purification of the amplicons was done using the Zymo DNA Clean & ConcentratorTM-5 Kit (Zymo Research, Irvine, CA, #ZY-D4013). Gel electrophoresis was performed on a FlashGelTM System (Lonza Group AG, Basel, Switzerland #57067) to check the binding of the primers and verify the amplicon length (see Supplementary Information S4).

2.5. Lambda exonuclease digestion

After PCR amplicon generation, the DNA concentration of the purified PCR product was determined using a NanoDropTM 1000 Spectrophotometer (Thermo Fisher Scientific), and the amplicons diluted to 10 ng/ μ L in a total reaction volume of 50 μ L containing 2 μ L of 1.25 U/ μ L Lambda exonuclease (Thermo Fisher Scientific, #EN0561) and 5 μ L of 10 \times supplied reaction buffer. The reaction mixture was heated to 37 $^{\circ}$ C for 30 min followed by 85 $^{\circ}$ C for 10 min on a VeritiTM 96-Well Thermal Cycler for the selective digestion of the 5'-phosphorylated strands to generate 107 bp long single-stranded DNA. The exonuclease digestion efficiency was previously confirmed by Van Hoof et al. (2022). Samples were stored at -20 $^{\circ}$ C and used without further purification.

2.6. DNA hybridization experiment

To perform the hybridization experiment for *EGFR* T790M detection, we used two custom $8 \times 15K$ Agilent microarray slides (Agilent Technologies, Santa Clara, CA, USA, #G2509F) with the same design as described in Van Hoof et al. (2022). Briefly, one slide contained 8 *EGFR* depletion arrays and the other contained 8 no-depletion arrays. Depletion was induced by introducing a large number of spots containing *Pwt* (14900 spots) on one of the arrays compared to *Pmut* (20 spots) and *Pref* (20 spots). The no-depletion array contained equal numbers of *Pwt*, *Pmut* and *Pref* (20 each). The 20 replicates determine the 95% confidence interval. The readout of the slides is presented in Supplementary Information S5. Oligonucleotide sequences are presented in Fig. 2D. The Gene Expression Microarrays Hybridization Kit (Agilent Technologies, #5188-5242) was used and the hybridization mixture contained: 25.0 μL of $2 \times \text{GEx}$ hybridization buffer, 5.0 μL $10 \times$ blocking agent, 3.5 μL of Lambda exonuclease-digested *EGFR* amplicons (1 nM for the depletion array and 0.01 nM for the no-depletion array), 2.0 μL 5' Cy-3 labeled barcode oligonucleotides (1250 nM, 5' -/5Cy3/AAA AAC TGG CGT CAT AGC TGT TTC CTG TGT GA -3') and 14.5 μL nuclease-free water in a total volume of 50 μL . Hybridization and washing were done according to the manufacturer's instructions. Briefly, 40 μL of hybridization mixture was placed on an 8-well gasket slide (Agilent Technologies, #G2534-60016) that was placed inside a hybridization chamber (Agilent Technologies, #G2534A). The microarray slide was placed on top (with the active side down), the hybridization chamber was closed with the chamber cover and the assembly was clamped in place. It was checked that there were no stationary bubbles present in the assembly. The hybridization chamber was placed inside a hybridization oven (Agilent Technologies, #G2545A) and rotated at 10 rpm at 65 °C for 17 h. Array scanning was performed on an Agilent G2565CA (G2505C) Series Microarray Scanner System and Scan Control Software A8.4.1 (Agilent Technologies) with settings for scan region: Agilent HD (61×21.5 mm), resolution: 5 μm , TIFF image: 20-bit, photomultiplier tube: 100% and no eXtended Dynamic Range feature. Agilent Feature Extraction Software 10.7.3.1 (Agilent Technologies) was used to analyze the array images with automatic gridding, intensity measurement, background subtraction and quality checks.

The 18 cfDNA samples were analyzed in three runs, each performed on the same slides after regeneration. Each run contained a negative control which was used for baseline subtraction, as was done by Van Hoof et al. (2022). Between each run, the two slides were regenerated by washing them for 44 min in a 1:1 mix of wash buffer 2 from the Gene Expression Microarrays Hybridization Kit with Milli-Q water at 65 °C and drying before storage at room temperature.

3. Results and discussion

3.1. Application to clinical samples

The sample set of this work consisted of 18 cfDNA samples from NSCLC patients. In general, these samples contained wild-type cfDNA and possibly a small fraction of tumor-originating *EGFR* T790M mutant cfDNA. All samples were tested for the presence of this point mutation in a clinically-validated real-time PCR assay. This assay relies on a ΔC_t value: the difference in PCR amplification cycles before it reaches a detection threshold between the mutation, *EGFR* T790M, and a housekeeping gene (see Section 2.2). A higher ΔC_t value corresponds to a lower mutant ratio. Both panels of Fig. 3 show the ΔC_t values on the (reversed) x -axis. Samples that did not reach the detection threshold for *EGFR* T790M after 40 PCR cycles were classified as negative and are indicated as NaN (Not a Number) since no ΔC_t value could be calculated. Samples with $\Delta C_t \geq 7.4$ were above the clinical threshold and classified as negative (12 samples), and samples with $\Delta C_t \leq 7.4$ were classified as positive (6 samples).

Next, the set of 18 samples was evaluated using the hybridization assay of Section 2.1. This assay is thermodynamics-based, it uses DNA probes to capture specific target sequences in the sample and the resulting readout is determined by hybridization free-energy parameters of the sequences at hand, and by the ratio c_{mut}/c_{wt} , i.e. the mutant over the wild-type cfDNA concentration in the sample. The assay signal provides a quantitative measurement of the mutant ratio c_{mut}/c_{wt} (see Fig. 2C and Eqs. (4) and (5)). The hybridization assay was developed in a no-depletion and a depletion version. The latter depletes the wild-type cfDNA in the sample leading to an improved LoD for the mutant ratio (see Section 2.1.3 for details and numerical values). When a mutant ratio is below LoD, it is classified as negative and represented by zero on Fig. 3. The resulting values are presented on the y -axis of Fig. 3.

We observed a correlation between ΔC_t values and mutant ratios c_{mut}/c_{wt} of both hybridization assay variants for the clinically positive samples. For samples that were clinically assigned as negative, the majority was also negative (i.e. below LoD) in both hybridization assays. Hence, there was a general concordance between the clinical PCR and the hybridization assays. However, there were some interesting exceptions. Both hybridization assays detected the mutation in sample 18 (further discussed in Section 3.2) whereas no mutation was detected using real-time PCR. Samples 12 and 15 have a $\Delta C_t \geq 7.4$, hence clinically classified negative, but received a non-zero mutant ratio c_{mut}/c_{wt} above the LoD in the depletion hybridization assay. This suggested that these samples could contain a low number of mutant targets. Further, the real-time PCR assay was not able to measure a ΔC_t value for samples 8 and 16 (assigned NaN), but again, the depletion hybridization assay detected a non-zero mutant concentration.

3.2. Evaluation of the quantitative agreement with dPCR

Since real-time PCR does not provide an absolute quantitative description of the mutant fraction in a sample, we performed also dPCR measurements on the clinical samples. Digital PCR is a sensitive technique for absolute quantification and regarded as the gold-standard for low-abundant mutant detection (Silveira et al., 2021; Zhang et al., 2015). All 18 clinical samples were run in a dPCR assay as described in Section 2.3. The assay has a technical control criterion, stating that the droplet count has to be $\geq 10,000$ droplets/well. This inclusion criterion resulted in the rejection for further analysis of samples 3, 7 and 8. For all other samples a mutant ratio c_{mut}/c_{wt} was determined by dPCR, and compared with those of the two hybridization assays (Fig. 4).

Firstly, the samples which are classified as positive by the clinical assay (real-time PCR, Fig. 3) all show a strong quantitative correlation between the dPCR and hybridization assays with Pearson correlation coefficient of 0.89 and 0.84 for the no-depletion and depletion assays, respectively. Despite this correlation, it was found that the depletion assay underestimated the mutant ratio, which is further examined in the next section. Also, samples 2, 4, 5 and 6 were in full agreement, i.e. no mutant detected. Next, samples 12 and 16 were negatively classified by the clinical assay but showed the presence of the mutation in the depletion hybridization assay which was confirmed by the dPCR. These results showed the increased sensitivity of the depletion assay over the no-depletion assay, and confirmed that the outcome of the hybridization assays, developed on synthetic DNA, can be translated to clinical samples and lead to improved diagnostics of SNV mutations.

Furthermore, the samples in subset 9, 15, 17 and 18 (each indicated by a triangle in Fig. 4) were around the detection limit of the dPCR: these samples had only one or two mutant-positive droplets, which is below the three positive droplets generally adopted as a cut-off for positivity in good practice according to the manufacturer (Bio-Rad Laboratories Inc., 2015). Of this subset, samples 9 and 17 were negative across all other analysis methods, indicating that either dPCR detected a very low abundance of mutants, or the mutant-positive droplets were false positives. A single mutant-positive droplet was detected in sample 18, but the measured mutant ratio by dPCR was

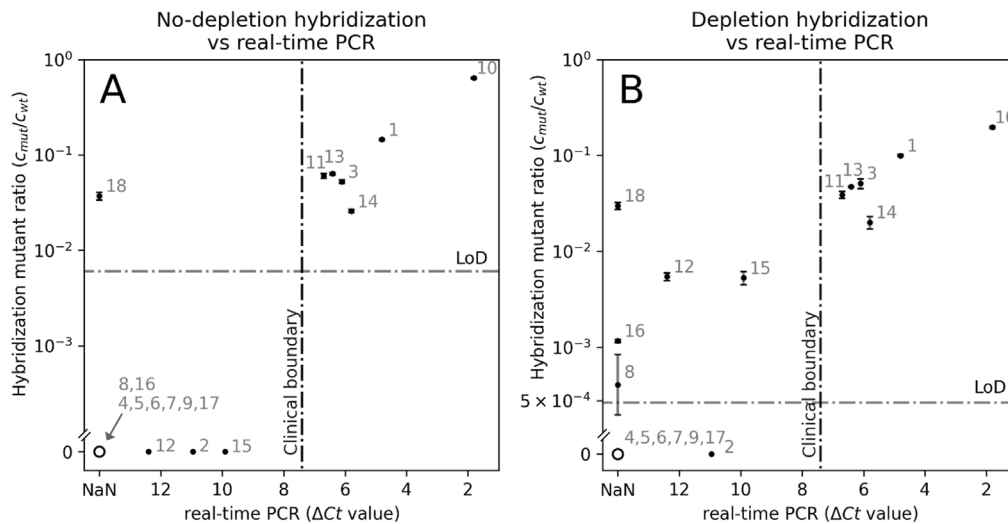


Fig. 3. Scatter plot of mutant ratios c_{mut}/c_{wt} obtained by the hybridization assay under no-depletion condition (A) and depletion condition (B) versus ΔCt values obtained by real-time PCR for 18 cfDNA samples from NSCLC patients. Errorbars show the 95% confidence interval. Horizontal dashed lines represent the respective LoD for each hybridization assay condition. Vertical dashed lines represent the clinical threshold between positive and negative samples for the real-time PCR assay. Samples that were both below the LoD and had no ΔCt value (NaN) are depicted with an open circle symbol.

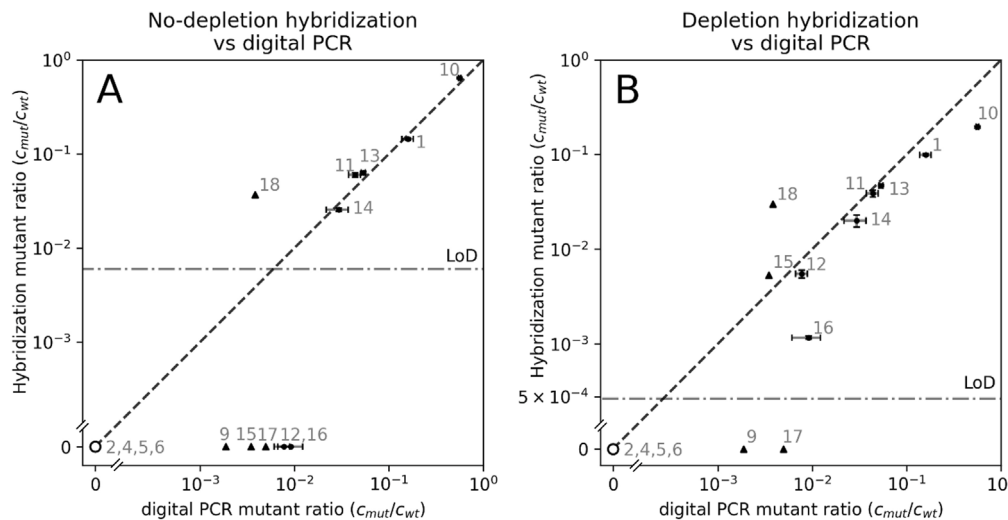


Fig. 4. Scatter plot of mutant ratios c_{mut}/c_{wt} obtained by the hybridization assay under no-depletion condition (A) and depletion condition (B) versus dPCR for 18 cfDNA samples from NSCLC patients (1-18). Errorbars show the 95% confidence interval. A dashed diagonal is shown as a visual guide. Horizontal dashed lines represent the respective LoD for each hybridization assay condition. Samples are shown as dots, except when the number of mutant positive droplets < 3, in which case they are denoted with a triangle. Samples 3, 7 and 8 did not meet the technical control criterion for dPCR and are not shown. The open circle symbol represents cases for which no mutant was detected in both the hybridization assays and dPCR.

lower than the expected ratio from the hybridization assay. Since in both hybridization assays the mutant ratios in sample 18 were equally high and well above the LoD, we suspected that the observed ratio in the hybridization assay was the result of sample contamination. Sample 15 was negative in the no-depletion hybridization assay, positive in the depletion hybridization assay, and received a ΔCt value in the real-time PCR, which suggested a positive but very low mutant content.

3.3. Extension of the model to accurately determine high mutant concentrations

In the previous section, we compared the difference between the two hybridization assays for positively classified samples. While both correlated well with the dPCR (Fig. 4), the depletion assay underestimates the mutant ratio. This issue is due to an interaction not taken into account in the theory of Section 2.1. This interaction will be discussed below and lead to an extension of the theory of Section 2.1.

The extension to the model will result in a more accurate description of the signal for high mutant ratios, and consequently, high mutant ratios are more accurately quantified.

The mutant ratios from the depletion and no-depletion assays are plotted in Fig. 5A. Again, this figure shows the concordance between the two assays for the majority of the samples and the improved LoD for the depletion assay, visible for samples 8, 12, 15, and 16. A clear correlation is visible in the upper-right quadrant. However, depletion-derived values are lower than no-depletion, and an apparent deviation from the diagonal is visible at the highest mutant ratios.

To address this issue, we re-evaluate the data analysis which leads to the mutant ratio c_{mut}/c_{wt} . Fig. 2C illustrates how, for both the depletion and no-depletion method, a measurement leads to the determination of the mutant ratio in a sample. When theory and experiment match, the two assays agree on the amount of mutants in the sample.

Using Eqs. (4) and (5), the same was done for the clinical samples on Fig. 5C. The experimental signal is plotted on the y-axis versus

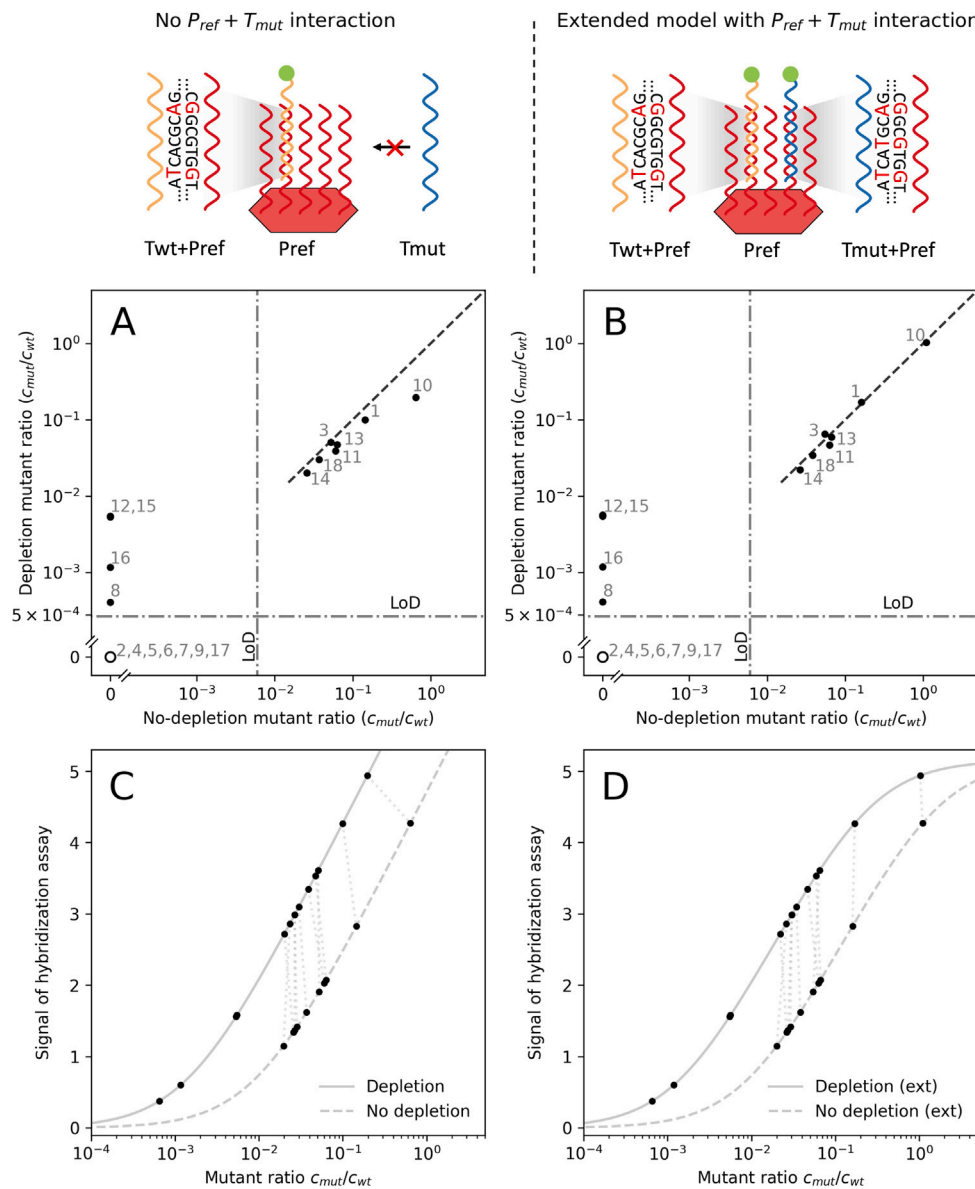


Fig. 5. The effect of the extension of the thermodynamic hybridization model. The binding of the mutant target to the reference probe is neglected in (A) and (C) or taken into account in (B) and (D). (A) and (B) Scatter plots of mutant ratios c_{mut}/c_{wt} obtained by the two hybridization assays with and without wild-type target depletion. Horizontal and vertical lines represent the LoD for the depletion and no-depletion assay condition, respectively. The open circle symbol represents cases for which no mutant was detected using both the hybridization conditions. (C) and (D) Determination of mutant ratio c_{mut}/c_{wt} from the signal without (C) and with (D) taking into account the mutant target (T_{mut})-reference probe (P_{ref}) interaction. Solid curves represent Eqs. (2) and (3) (C), and (7) and (8) (D). For both depletion and no-depletion hybridization conditions, the experimental signal is plotted on the y-axis against the calculated mutant ratio. The dotted lines connect corresponding samples for the depletion and no-depletion assay.

the derived mutant ratio on the x-axis for both depletion and no-depletion. Corresponding samples for depletion and no-depletion assays are connected by dashed lines, which should be vertical when theory and experiment match. The discrepancy between the two assays is apparent for samples with a high mutant fraction. This observation points to the solution of the issue: the physical model used in Fig. 5C (see Section 2.1) was developed to accurately describe samples with low mutant fractions. In this limit, it is correct to neglect the interaction between T_{mut} and the reference probe P_{ref} . Since the mutant ratio in some of the current samples is higher than those used in the work of Van Hoof et al. (2022), the interaction of the mutant target with the reference probe cannot be neglected for these samples. Intuitively, while for low mutant ratios, the reference probe intensity can be considered approximately constant and only dependent on the amount of T_{wt} , the intensity of the reference probe at high c_{mut}/c_{wt} is

dependent on both the amount of T_{wt} and T_{mut} in the sample. The observed discrepancy between the depletion and no-depletion assay is then understood by the fact that the effect occurs at lower c_{mut}/c_{wt} values for the depletion assay, because this assay actively changes the ratio of T_{mut} over T_{wt} in the sample.

For a quantitative description we extended the applicability range of the physical hybridization model by incorporating all target interactions with P_{ref} . A detailed derivation of the extended theory is provided in the Supplementary Information S6. The extension adds an additional term to Eqs. (2) and (3), leading to:

No-depletion:

$$S_{no_depl} = \ln \left(1 + \frac{c_{mut}}{c_{wt}} \exp \left(\frac{\Delta\Delta G_{P_{mut}}}{RT} \right) \right) - \ln \left(1 + \frac{c_{mut}}{c_{wt}} \exp \left(\frac{\Delta\Delta G_{P_{ref}}}{RT} \right) \right) \quad (7)$$

Table 1

Overview of free-energy parameters relevant in the hybridization assay. Van Hoof et al. (2022) determined the thermodynamic parameters from synthetic samples at low mutant ratios. Adding $\Delta\Delta G_{Pmut}$ to $\Delta\Delta G_{Pref} - \Delta\Delta G_{Pmut}$ results in an estimation of the reference probe interaction $\Delta\Delta G_{Pref}$, as presented in the last column.

Free-energy parameter	Fit to clinical data		Van Hoof et al. (2022)		Reference probe interaction
	$\frac{\Delta\Delta G_{Pwt}}{RT}$	$\frac{\Delta\Delta G_{Pref} - \Delta\Delta G_{Pmut}}{RT}$	$\frac{\Delta\Delta G_{Pwt}}{RT}$	$\frac{\Delta\Delta G_{Pmut}}{RT}$	$\frac{\Delta\Delta G_{Pref}}{RT}$
Value	1.80 ± 0.06	-5.15 ± 0.17	1.86 ± 0.15	4.7 ± 0.1	-0.45 ± 0.27

Depletion:

$$S_{depl} = \ln \left(1 + \frac{c_{mut}}{c_{wt}} \exp \left(\frac{\Delta\Delta G_{Pmut} + \Delta\Delta G_{Pwt}}{RT} \right) \right) - \ln \left(1 + \frac{c_{mut}}{c_{wt}} \exp \left(\frac{\Delta\Delta G_{Pref} + \Delta\Delta G_{Pwt}}{RT} \right) \right) \quad (8)$$

where the extra parameter $\Delta\Delta G_{Pref}$ represents the target interactions with *Pref*. Specifically, $\Delta\Delta G_{Pref}$ is the difference in hybridization free energy between the reference probe and the two targets, $\Delta G(Pref + Twt) - \Delta G(Pref + Tmut)$. Since *Pref* + *Tmut* contains an additional mismatch (see Fig. 5), $\Delta\Delta G_{Pref}$ is negative.

The additional terms in Eqs. (7) and (8) are not identical, which explains quantitatively the discrepancy between the two assays. More specifically, for the depletion assay, the depletion interaction $\Delta\Delta G_{Pwt}$ is present in the additional term, which is why the new interaction has a larger influence in the case of depletion. When all free-energy differences are known, similar to Section 2.1.3, the mutant ratio of a sample is obtained by inverting Eqs. (7) and (8). The resulting equations are provided in Supplementary Information S7.

The effect of the extended model is visible in Fig. 5B, where (as opposed to Fig. 5A) the depletion and no-depletion assays now agree on the amount of mutants in the samples. The dynamic range is enlarged ~10-fold by including the *Pref* + *Tmut* interaction. The extension of the model is also illustrated by the solid curves of Fig. 5D: for high mutant ratios the signal curves flatten out, i.e. they become sigmoidal. For small mutant ratios the curves of Fig. 5C and 5D remain identical. The additional subtraction in Eqs. (7) and (8) becomes important for high mutant ratios, where the signal was overestimated and therefore the predicted mutant ratio was underestimated. Hence, the extension allows for a more accurate determination of the amount of mutant in a sample, relevant at high mutant ratios, by introducing a single extra free-energy parameter $\Delta\Delta G_{Pref}$ with a clear physical meaning.

The parameter $\Delta\Delta G_{Pref}$ can be extracted from the data. Any sample that is measured in both the depletion and no-depletion conditions contains the same amount of mutant for both conditions. Eliminating c_{mut}/c_{wt} from Eqs. (7) and (8) provides a mapping of the depletion signal onto the no-depletion signal for the same sample. This curve can be fitted for the values of $\Delta\Delta G_{Pwt}$ and $\Delta\Delta G_{Pref} - \Delta\Delta G_{Pmut}$. Since $\Delta\Delta G_{Pmut}$ is known from previous work by Van Hoof et al. (2022), this allows the value of $\Delta\Delta G_{Pref}$ to be determined. The derivation, along with the fitting procedure can be found in Supplementary Information S8. The free-energy values are summarized in Table 1. The fit provides a way to determine $\Delta\Delta G_{Pref}$. By adding the value of $\Delta\Delta G_{Pmut}/RT = 4.7$, we obtain $\Delta\Delta G_{Pref}/RT = -0.45$ as presented in the last column. Note that the fitted value of the wild-type probe parameter $\Delta\Delta G_{Pwt}$ provides an independent determination of this free-energy difference. The agreement with the value reported by Van Hoof et al. (2022) shows the consistency of the hybridization method and the fitting procedure.

It is instructive to compare the value of $\Delta\Delta G_{Pref}$ with the theoretical value of a simple nearest-neighbor model for hybridization free energy (Hadiwikarta et al., 2012). The nearest-neighbor calculation predicts a value of -2.3 for $\Delta\Delta G_{Pref}/RT$. The measured value (Table 1) is noticeably smaller. This can be understood by identifying the locations of the mismatches present in the *Tmut* + *Pref* binding (Fig. 5). Three mismatches are present in close proximity of each other, only being separated by two nucleotide pairs that obey the Watson-Crick pairing rule. It is known that, when the distance between two mismatches is closer than five nucleotides, the additivity principle,

which is the basis of the nearest-neighbor model, breaks down, and the model overestimates the free-energy penalty (Hadiwikarta et al., 2012). This effect becomes even more pronounced when three mismatches are near each other, as is the case for the mutant-reference probe interaction. The overestimation (more negative) of $\Delta G(Pref + Tmut)$ implies $\Delta\Delta G_{Pref}/RT > -2.3$, which explains the observed value presented in Table 1. The *Tmut* + *Pref* binding is therefore more stable than predicted using the nearest-neighbor model because the mismatches are in close proximity of each other. As a result, the *Tmut* + *Pref* interaction, which can be seen as a flattening of the curve due to a lower increase in the signal, occurs at a lower mutant ratio than expected without accounting for the proximity of the mismatches. This thermodynamic insight leads to an important design concept for future reference probes, namely that the additional mismatch of the reference probe to *Tmut* compared to *Twt* is ideally separated more than five nucleotides from the mismatches already present in *Pref* + *Twt* in order to maximize the free energy penalty.

The determined value of the physical parameter $\Delta\Delta G_{Pref}$ can now be used in our extended model to accurately determine the mutant ratio in the hybridization assay. The signal as a function of c_{mut}/c_{wt} for the extended model is shown in Fig. 5D. The extension resolves the disagreement between depletion and no-depletion results, and agreement is observed in Fig. 5B. We finally note that the theoretical extension and the addition of parameter $\Delta\Delta G_{Pref}$ are important only at high mutant ratios, where it allows a more accurate determination of the mutant ratio, and the extension has a negligible effect on samples with a low mutant ratio and the analysis of the previous sections is retained.

4. Conclusions

We have successfully applied the thermodynamics-based concept of wild-type target depletion to clinical circulating free DNA samples using a hybridization assay for single nucleotide variation detection, demonstrating a 10-fold increase in sensitivity. We found an agreement between our data and the qualitative results of a clinically-validated assay, as well as a quantitative agreement on mutant ratios present in the samples compared to digital PCR. By incorporating all relevant molecular interactions in the thermodynamic model, we enlarged the dynamic range within which a quantitative determination of the mutant ratio can be obtained by a factor 10. The assay therefore becomes suitable for both sensitive detection of low mutant levels in early diagnosis as well as the accurate determination of high mutant abundances which are clinically relevant e.g. in the follow-up of advanced cancer. In addition, the thermodynamic analysis gave insight into future reference probe designs. The possibility for parallel detection of multiple nucleotide variants needs to be further explored since parallelization is a strength of the hybridization technology.

Our thermodynamic approach starts from physicochemical properties of DNA and is independent of the readout system of the used sensor. It can therefore be applied to a wide range of hybridization-based biosensing technologies and platforms, including cost-effective sensors operable at room temperature. This method can be utilized as a multiplex platform for the simultaneous detection of various single nucleotide variations (SNVs) using the same depletion mechanism and reference probe. Supplementary Information S9 outlines the steps required to transfer the hybridization method to alternative platforms or to modify the design for detecting different target sequences. It is a robust and effective method to improve the performance of existing biosensors which currently lack the sensitivity required for the analysis of single nucleotide variations.

CRediT authorship contribution statement

Yannick Stulens: Writing – original draft, Methodology, Investigation, Data curation. **Rebekka Van Hoof:** Writing – original draft, Resources, Methodology, Investigation, Data curation. **Karen Hollanders:** Methodology, Investigation, Data curation. **Inge Nelissen:** Writing – review & editing, Resources, Methodology, Investigation, Funding acquisition, Data curation, Conceptualization. **Michal Szymonik:** Writing – review & editing, Methodology, Investigation, Data curation. **Patrick Wagner:** Writing – review & editing, Funding acquisition, Conceptualization. **Guy Froyen:** Writing – review & editing, Resources. **Brigitte Maes:** Writing – review & editing, Resources. **Jef Hooyberghs:** Writing – original draft, Supervision, Methodology, Investigation, Funding acquisition, Data curation, Conceptualization.

Ethical approval

The study was conducted in accordance with the Declaration of Helsinki, and approved by the Ethics Review Committee of the Jessa Hospital (protocol code 2021/023, 08/09/2021). Patient consent was waived due to the fact that only residual material was used for this study.

Funding

This work was supported by the Research Foundation Flanders (FWO) 1S69320N/1S69322N; Special Research Fund BOF220WB11; EU H2020 M3DLoC project 760662 and VITO nv.

Declaration of competing interest

The authors declare that they have no known competing financial interests or personal relationships that could have appeared to influence the work reported in this paper.

Appendix A. Supplementary data

Supplementary material related to this article can be found online at <https://doi.org/10.1016/j.bios.2025.117342>.

Data availability

Data is provided in the Supplementary Information.

References

- Abbosh, C., Birkbak, N.J., Wilson, G.A., Jamal-Hanjani, M., Constantin, T., Salari, R., Le Quesne, J., Moore, D.A., Veeriah, S., Rosenthal, R., Marafioti, T., Kirkizlar, E., Watkins, T.B.K., McGranahan, N., Ward, S., Martinson, L., Riley, J., Fraioli, F., Al Bakir, M., Grönroos, E., Zambrana, F., Endozo, R., Bi, W.L., Fennessy, F.M., Sporer, N., Johnson, D., Laycock, J., Shafi, S., Czyżewska-Khan, J., Rowan, A., Chambers, T., Matthews, N., Turajlic, S., Hiley, C., Lee, S.M., Forster, M.D., Ahmad, T., Falzon, M., Borg, E., Lawrence, D., Hayward, M., Kolvekar, S., Panagiotopoulos, N., Janes, S.M., Thakrar, R., Ahmed, A., Blackhall, F., Summers, Y., Hafez, D., Naik, A., Ganguly, A., Kareht, S., Shah, R., Joseph, L., Marie Quinn, A., Crosbie, P.A., Naidu, B., Middleton, G., Langman, G., Trotter, S., Nicolson, M., Remmen, H., Kerr, K., Chetty, M., Gomersall, N., Gomersall, D.A., Nakas, A., Rathinam, S., Anand, G., Khan, S., Russell, P., Ezhil, V., Ismail, B., Irvin-Sellers, M., Prakash, V., Lester, J.F., Kornaszewska, M., Attanoos, R., Adams, H., Davies, H., Oukrif, D., Akarca, A.U., Hartley, J.A., Lowe, H.L., Lock, S., Iles, N., Bell, H., Ngai, Y., Elgar, G., Szallasi, Z., Schwarz, R.F., Herrero, J., Stewart, A., Quezada, S.A., Peggs, K.S., Van Loo, P., Dive, C., Lin, C.J., Rabinowitz, M., Aerts, H.J.W.L., Hackshaw, A., Shaw, J.A., Zimmermann, B.G., Swanton, C., 2017. Phylogenetic ctDNA analysis depicts early-stage lung cancer evolution. *Nature* 545 (7655), 446–451, URL: <https://www.nature.com/articles/nature22364>. Publisher: Nature Publishing Group.
- Alese, O.B., Cook, N., Ortega-Franco, A., Ulanja, M.B., Tan, L., Tie, J., 2022. Circulating tumor DNA: An emerging tool in gastrointestinal cancers. *Am. Soc. Clin. Oncol. Educ. Book* (42), 279–298, URL: <https://ascopubs.org/doi/10.1200/EDBK.349143>.

- Alexandrou, G., Mantikas, K.-T., Allsopp, R., Yapeter, C.A., Jahin, M., Melnick, T., Ali, S., Coombes, R.C., Toumazou, C., Shaw, J.A., Kalofonou, M., 2023. The evolution of affordable technologies in liquid biopsy diagnostics: The key to clinical implementation. *Cancers* 15 (22), 5434, URL: <https://www.ncbi.nlm.nih.gov/pmc/articles/PMC10670715/>.
- Alipour, M., Jalili, S., Shirzad, H., Ansari Dezfouli, E., Fouani, M.H., Sadeghan, A.A., Bardania, H., Hosseinkhani, S., 2020. Development of dual-emission cluster of Ag atoms for genetically modified organisms detection. *Microchim. Acta* 187 (11), 628. <http://dx.doi.org/10.1007/s00604-020-04591-2>.
- Bio-Rad Laboratories Inc., 2015. Bulletin.6407.pdf (accessed in June 2024). Droplet Digit. PCR Appl. Guid. URL: https://www.bio-rad.com/webroot/web/pdf/lst/literature/Bulletin_6407.pdf.
- Cohen, S.A., Liu, M.C., Aleshin, A., 2023. Practical recommendations for using ctDNA in clinical decision making. *Nature* 619 (7969), 259–268, URL: <https://www.nature.com/articles/s41586-023-06225-y>. Publisher: Nature Publishing Group.
- Dillen, A., Mohrbacher, A., Lammertyn, J., 2021. A versatile one-step competitive fiber optic surface plasmon resonance bioassay enabled by DNA nanotechnology. *ACS Sensors* 6 (10), 3677–3684. <http://dx.doi.org/10.1021/acssensors.1c01447>, Publisher: American Chemical Society.
- Ferrara, F., Zoupanou, S., Primiceri, E., Ali, Z., Chiriaco, M.S., 2022. Beyond liquid biopsy: Toward non-invasive assays for distant cancer diagnostics in pandemics. *Biosens. Bioelectron.* 196, 113698, URL: <https://www.sciencedirect.com/science/article/pii/S0956566321007351>.
- García-Pardo, M., Makarem, M., Li, J.J.N., Kelly, D., Leighl, N.B., 2022. Integrating circulating-free DNA (cfDNA) analysis into clinical practice: opportunities and challenges. *Br. J. Cancer* 127 (4), 592–602, URL: <https://www.nature.com/articles/s41416-022-01776-9>. Publisher: Nature Publishing Group.
- Hadiwikarta, W.W., Walter, J.-C., Hooyberghs, J., Carlon, E., 2012. Probing hybridization parameters from microarray experiments: nearest-neighbor model and beyond. *Nucleic Acids Res.* 40 (18), e138. <http://dx.doi.org/10.1093/nar/gks475>.
- Harrison, A., Binder, H., Buhot, A., Burden, C.J., Carlon, E., Gibas, C., Gamble, L.J., Halperin, A., Hooyberghs, J., Kreil, D.P., Levicky, R., Noble, P.A., Ott, A., Pettitt, B.M., Tautz, D., Pozhitkov, A.E., 2013. Physico-chemical foundations underpinning microarray and next-generation sequencing experiments. *Nucleic Acids Res.* 41 (5), 2779–2796. <http://dx.doi.org/10.1093/nar/gks1358>.
- Hooyberghs, J., Baiesi, M., Ferrantini, A., Carlon, E., 2010. Breakdown of thermodynamic equilibrium for DNA hybridization in microarrays. *Phys. Rev. E* 81 (1), 012901, URL: <https://link.aps.org/doi/10.1103/PhysRevE.81.012901>. Publisher: American Physical Society.
- Karadeema, R.J., Stancescu, M., Steidl, T.P., Bertot, S.C., Kolpashchikov, D.M., 2018. The owl sensor: a ‘fragile’ DNA nanostructure for the analysis of single nucleotide variations. *Nanoscale* 10 (21), 10116–10122, URL: <https://pubs.rsc.org/en/content/articlelanding/2018/nr/c8nr01107a>. Publisher: The Royal Society of Chemistry.
- Knez, K., Spasic, D., Janssen, K.P.F., Lammertyn, J., 2013. Emerging technologies for hybridization based single nucleotide polymorphism detection. *Analyst* 139 (2), 353–370, URL: <https://pubs.rsc.org/en/content/articlelanding/2014/an/c3an01436c>. Publisher: The Royal Society of Chemistry.
- Li, X., Ye, M., Zhang, W., Tan, D., Jaffrezic-Renault, N., Yang, X., Guo, Z., 2019. Liquid biopsy of circulating tumor DNA and biosensor applications. *Biosens. Bioelectron.* 126, 596–607, URL: <https://www.sciencedirect.com/science/article/pii/S0956566318309321>.
- Lino, C., Barrias, S., Chaves, R., Atega, F., Martins-Lopes, P., Fernandes, J.R., 2022. Biosensors as diagnostic tools in clinical applications. *Biochim. et Biophys. Acta (BBA) - Rev. Cancer* 1877 (3), 188726, URL: <https://www.sciencedirect.com/science/article/pii/S0304419X22000518>.
- Lu, J., Feng, Y., Guo, K., Sun, L., Ruan, S., Zhang, K., 2024. Prognostic value of preoperative circulating tumor DNA in non-small cell lung cancer: a systematic review and meta-analysis. *J. Cancer Res. Clin. Oncol.* 150 (1), 25.
- Magar, H.S., Hassan, R.Y.A., Mulchandani, A., 2021. Electrochemical impedance spectroscopy (EIS): Principles, construction, and biosensing applications. *Sensors* 21 (19), 6578, URL: <https://www.mdpi.com/1424-8220/21/19/6578>. Number: 19 Publisher: Multidisciplinary Digital Publishing Institute.
- Mueller, B.L., Liberman, M.J., Kolpashchikov, D.M., 2023. OWL2: a molecular beacon-based nanostructure for highly selective detection of single-nucleotide variations in folded nucleic acids. *Nanoscale* 15 (12), 5735–5742, URL: <https://pubs.rsc.org/en/content/articlelanding/2023/nr/d2nr05590b>. Publisher: The Royal Society of Chemistry.
- Nomidis, S.K., Szymonik, M., Venken, T., Carlon, E., Hooyberghs, J., 2019. Enhancing the performance of DNA surface-hybridization biosensors through target depletion. *Langmuir* 35 (37), 12276–12283. <http://dx.doi.org/10.1021/acs.langmuir.9b01761>, Publisher: American Chemical Society.
- Silveira, C., Sousa, A.C., Janeiro, A., Malveiro, S., Teixeira, E., Brysch, E., Pantarotto, M., Felizardo, M., Madureira, R., Nogueira, F., Guimarães, C., Matos, C., Canário, D., Bruges-Armas, J., Carmo-Fonseca, M., 2021. Detection and quantification of EGFR T790M mutation in liquid biopsies by droplet digital PCR. *Transl. Lung Cancer Res.* 10 (3), 1200–1208, URL: <https://www.ncbi.nlm.nih.gov/pmc/articles/PMC8044487/>.
- Sivapalan, L., Murray, J.C., Canzoniero, J.V., Landon, B., Jackson, J., Scott, S., Lam, V., Levy, B.P., Sausen, M., Anagnostou, V., 2023. Liquid biopsy approaches to capture tumor evolution and clinical outcomes during cancer immunotherapy. *J. Immunother. Cancer* 11 (1), e005924.

- Takahashi, H., Yasui, T., Hirano, M., Shinjo, K., Miyazaki, Y., Shinoda, W., Hasegawa, T., Natsume, A., Kitano, Y., Ida, M., Zhang, M., Shimada, T., Paisrisarn, P., Zhu, Z., Ohka, F., Aoki, K., Rahong, S., Nagashima, K., Yanagida, T., Baba, Y., 2023. Mutation detection of urinary cell-free DNA via catch-and-release isolation on nanowires for liquid biopsy. *Biosens. Bioelectron.* 234, 115318, URL: <https://www.sciencedirect.com/science/article/pii/S0956566323002609>.
- Udomruk, S., Orrapin, S., Pruksakorn, D., Chaiyawat, P., 2021. Size distribution of cell-free DNA in oncology. *Crit. Rev. Oncol. Hematol.* 166, 103455, URL: <https://www.sciencedirect.com/science/article/pii/S1040842821002432>.
- Van Grinsven, B., Vanden Bon, N., Grieten, L., Murib, M., Janssens, S.D., Haenen, K., Schneider, E., Ingebrandt, S., Schöning, M.J., Vermeeren, V., Ameloot, M., Michiels, L., Thoelen, R., De Ceuninck, W., Wagner, P., 2011. Rapid assessment of the stability of DNA duplexes by impedimetric real-time monitoring of chemically induced denaturation. *Lab A Chip* 11 (9), 1656–1663, URL: <https://pubs.rsc.org/en/content/articlelanding/2011/lc/cl1c20027e>. Publisher: The Royal Society of Chemistry.
- Van Grinsven, B., Vanden Bon, N., Strauven, H., Grieten, L., Murib, M., Jiménez Monroy, K.L., Janssens, S.D., Haenen, K., Schöning, M.J., Vermeeren, V., Ameloot, M., Michiels, L., Thoelen, R., De Ceuninck, W., Wagner, P., 2012. Heat-transfer resistance at solid–liquid interfaces: A tool for the detection of single-nucleotide polymorphisms in DNA. *ACS Nano* 6 (3), 2712–2721. <http://dx.doi.org/10.1021/nl300147e>, Publisher: American Chemical Society.
- Van Hoof, R., Szymonik, M., Nomidis, S.K., Hollanders, K., Jacobs, A., Nelissen, I., Wagner, P., Hooyberghs, J., 2022. Depletion of wild-type target enhances the hybridization-based sensitivity of low-abundant mutation detection by reference capture probes. *Sensors Actuators B: Chem.* 368, 132175, URL: <https://www.sciencedirect.com/science/article/pii/S0925400522008176>.
- Wang, S., Cang, S., Liu, D., 2016. Third-generation inhibitors targeting EGFR T790M mutation in advanced non-small cell lung cancer. *J. Hematol. Oncol.* 9 (1), 34. <http://dx.doi.org/10.1186/s13045-016-0268-z>.
- Wang, N., Zhang, X., Wang, F., Zhang, M., Sun, B., Yin, W., Deng, S., Wan, Y., Lu, W., 2021. The diagnostic accuracy of liquid biopsy in EGFR-mutated NSCLC: A systematic review and meta-analysis of 40 studies. *SLAS Technol.* 26 (1), 42–54, URL: <https://www.sciencedirect.com/science/article/pii/S2472630322010834>.
- Wei, F., Yu, P., Cheng, J., Li, F., Chia, D., Wong, D.T.W., 2023. Single-droplet microsensor for ultra-short circulating EGFR mutation detection in lung cancer based on multiplex EFIRM liquid biopsy. *Int. J. Mol. Sci.* 24 (12), 10387, URL: <https://www.mdpi.com/1422-0067/24/12/10387>. Number: 12 Publisher: Multidisciplinary Digital Publishing Institute.
- Willems, H., Jacobs, A., Hadiwikarta, W.W., Venken, T., Valkenburg, D., Van Roy, N., Vandesompele, J., Hooyberghs, J., 2017. Thermodynamic framework to assess low abundance DNA mutation detection by hybridization. *PLOS ONE* 12 (5), e0177384, URL: <https://journals.plos.org/plosone/article?id=10.1371/journal.pone.0177384>. Publisher: Public Library of Science.
- Wood, H.N., Venken, T., Willems, H., Jacobs, A., Reis, A.J., Almeida da Silva, P.E., Homolka, S., Niemann, S., Rohde, K.H., Hooyberghs, J., 2019. Molecular drug susceptibility testing and strain typing of tuberculosis by DNA hybridization. *PLoS One* 14 (2), e0212064, URL: <https://pubmed.ncbi.nlm.nih.gov/30730960/>.
- Xie, W., Suryaprakash, S., Wu, C., Rodriguez, A., Fraterman, S., 2023. Trends in the use of liquid biopsy in oncology. *Nat. Rev. Drug Discov.* 22 (8), 612–613, URL: <https://www.nature.com/articles/d41573-023-00111-y>. Bandiera_abtest: a Cg.type: Biobusiness Briefs Publisher: Nature Publishing Group.
- Yoshimine, H., Sasaki, K., Furusawa, H., 2023. Pocketable biosensor based on quartz-crystal microbalance and its application to DNA detection. *Sensors* 23 (1), 281, URL: <https://www.mdpi.com/1424-8220/23/1/281>. Number: 1 Publisher: Multidisciplinary Digital Publishing Institute.
- Zhang, B., Xu, C.-W., Shao, Y., Wang, H.-T., Wu, Y.-F., Song, Y.-Y., Li, X.-B., Zhang, Z., Wang, W.-J., Li, L.-Q., Cai, C.-L., 2015. Comparison of droplet digital PCR and conventional quantitative PCR for measuring EGFR gene mutation. *Exp. Ther. Med.* 9 (4), 1383–1388, URL: <https://www.ncbi.nlm.nih.gov/pmc/articles/PMC4353752/>.
- Zhou, J., Mo, H., Hu, D., Zhao, X., Zhou, H., Pan, J., 2023. Association of ctDNA detection and recurrence assessment in patients with neoadjuvant treatment. *Cancer Med.* 12 (19), 19794–19806.
- Zhuang, J., Xia, L., Zou, Z., Yin, J., Lin, N., Mu, Y., 2022. Recent advances in integrated microfluidics for liquid biopsies and future directions. *Biosens. Bioelectron.* 217, 114715, URL: <https://www.sciencedirect.com/science/article/pii/S0956566322007552>.